Transient dynamics of a superconducting nonlinear oscillator

P. Bhupathi,[1,*] Peter Groszkowski,[2,†] M.P. DeFeo,[1] Matthew Ware,[1] Frank K. Wilhelm,[2,3] and B.L.T. Plourde[1]

[1] *Department of Physics, Syracuse University, Syracuse, New York 13244-1130*
[2] *Institute for Quantum Computing and Department of Physics and Astronomy, University of Waterloo, 200 University Ave W, Waterloo, ON, N2L 3G1, Canada*
[3] *Theoretical Physics, Saarland University, 66123 Saarbrücken, Germany*

(Dated: February 16, 2016)

We investigate the transient dynamics of a lumped-element oscillator based on a dc superconducting quantum interference device (SQUID). The SQUID is shunted with a capacitor forming a nonlinear oscillator with resonance frequency in the range of several GHz. The resonance frequency is varied by tuning the Josephson inductance of the SQUID with on-chip flux lines. We report measurements of decaying oscillations in the time domain following a brief excitation with a microwave pulse. The nonlinearity of the SQUID oscillator is probed by observing the ringdown response for different excitation amplitudes while the SQUID potential is varied by adjusting the flux bias. Simulations are performed on a model circuit by numerically solving the corresponding Langevin equations incorporating the SQUID potential at the experimental temperature and using parameters obtained from separate measurements characterizing the SQUID oscillator. Simulations are in good agreement with the experimental observations of the ringdowns as a function of applied magnetic flux and pulse amplitude. We observe a crossover between the occurrence of ringdowns close to resonance and adiabatic following at larger detuning from the resonance. We also discuss the occurrence of phase jumps at large amplitude drive. Finally, we briefly outline prospects for a readout scheme for superconducting flux qubits based on the discrimination between ringdown signals for different levels of magnetic flux coupled to the SQUID.

I. INTRODUCTION

Superconducting circuits composed of Josephson junctions have been the subject of intense research for the past few decades for their importance in understanding the fundamental aspects of quantum mechanics as well as for their potential application towards quantum information processing and computing [1, 2]. These μm-sized devices have been shown to exhibit macroscopic quantum tunneling [3, 4], quantized energy levels [5] and superposition of states in a quantum bit (qubit) [6–8]. A central application of Josephson devices, classical or quantum, [9] is measurement. There have been many advances in utilizing Josephson devices such as a dc superconducting quantum interference device (SQUID) for qubit readout [10–13]. In these experiments, the SQUID forms part of a resonant oscillator circuit that is coupled to a qubit. Some of these Josephson devices configured as amplifiers have approached the quantum limit in noise performance [14–23]. All of these applications of Josephson junctions depend at some level on the nonlinearity of the junction response.

In this paper we investigate the temporal dynamics of a nonlinear SQUID resonant circuit. Studies of nonlinear oscillator dynamics under continuous excitation have been done previously [15, 24–27], and, in fact, many types of superconducting qubits, such as the transmon [28] or the phase qubit [8], are nonlinear oscillators that are typically driven with resonant pulses. However, we are not aware of any experimental or theoretical work to date on the transient dynamics of nonlinear oscillators under pulsed excitation in the time domain. Here we present time domain measurements of the decaying voltage oscillations from the SQUID oscillator after a brief excitation. The SQUID potential, and hence the resonance frequency, can be tuned by changing either the bias flux or bias current; here we focus on the variation with respect to flux, while no dc bias current is applied.

The paper is organized as follows. We start with a brief theoretical background of SQUID oscillators in Sec. II. In Sec. III we describe the fabrication of a lumped element SQUID oscillator and experimental measurement scheme. Measurements in the frequency and time domains are presented in Sec. IV. A model of the electrical circuit is presented in Sec. V, which is then used to derive the equations of motion of the full system. These equations are then reduced, accounting for the physical parameters used, and after incorporating thermal effects, are solved numerically to obtain the free evolution of the system for different conditions corresponding to the experiment. The simulated ringdowns in the time domain as a function of flux bias and pulse amplitude are in good agreement with the observations, as is shown in Sec. VI. Finally, in Sec. VII, a scheme for using ringdown oscillations of a SQUID oscillator to read out a flux qubit is briefly discussed, followed by our conclusions in Sec. VIII.

* Present Address: Department of Physics, California Institute of Technology, Pasadena, CA 91125, USA
† Present Address: Department of Physics and Astronomy, Northwestern University, Evanston, IL 60208, USA

II. THEORETICAL BACKGROUND

At the heart of all these investigations is the Josephson junction, which behaves as a nonlinear LC-oscillator characterized by the plasma resonance [9, 29], $\omega_p = \sqrt{2\pi I_0/\Phi_0 C_J}$, where, I_0 is the critical current of the Josephson junction in parallel with its self-capacitance C_J and $\Phi_0 \equiv h/2e$ is the magnetic flux quantum. For typical parameters of the fabricated junctions, $\omega_p/2\pi$ is of the order of 100 GHz. When shunted by a large external capacitance however, the resonance frequency can be lowered to a few GHz for ease of performing experiments with an oscillator for coupling to a qubit or to fabricate a qubit itself.

In this paper we consider a dc SQUID, which has two identical junctions in parallel, symmetrically placed on a superconducting loop. The dynamics of such a SQUID, as shown in a circuit schematic of Fig. 1, can be described by a two-dimensional anharmonic potential $U(\varphi_+, \varphi_-)$ given by [9, 30]

$$\frac{U}{2E_J} = -i_b\varphi_+ - \cos\varphi_+ \cos\varphi_- + \frac{1}{\beta}(\varphi_- - \pi f_s)^2 \quad (1)$$

where $E_J = I_0\Phi_0/2\pi$ is the Josephson coupling energy normalizing U, $L_{J0} = \Phi_0/2\pi I_0$ is the Josephson inductance of each junction, $\beta = 2\pi I_0 L_g/\Phi_0 = L_g/L_{J0}$ is the screening parameter of the SQUID with geometric loop inductance L_g, $i_b = I_b/2I_0$ is the bias current normalized by the critical current, and $f_s = \Phi_s/\Phi_0$ is the normalized applied flux. $\varphi_+ = (\varphi_A + \varphi_B)/2$ and $\varphi_- = (\varphi_A - \varphi_B)/2$ are the two independent degrees of freedom with φ_A and φ_B corresponding to the phase differences across each of the two Josephson junctions (see Fig. 5(a) and Appendix A for a more complete description of the SQUID potential energy and the rest of the circuit). The sum of the phases across the junctions (external mode), φ_+, couples to the current through the SQUID, while the difference of the phases (internal mode), φ_-, couples to the magnetic flux applied to the SQUID. The oscillator can be resonantly excited by applying a short alternating current pulse to the SQUID. The pulse perturbs the potential minimum of the SQUID, giving rise to oscillations of the phase particle about the minimum that decay at the characteristic frequency of the oscillator. The ringdown motion is mediated via the external mode of the oscillator and can be detected as a voltage oscillation across the SQUID.

III. EXPERIMENTAL SETUP

We investigate a lumped-element microwave oscillator circuit consisting of a dc SQUID shunted by a capacitor formed from superconducting layers. A circuit schematic and an optical micrograph of the device are shown in Fig. 1. A microwave feedline with on-chip capacitors couples signals into and out of the oscillator. Adjusting the bias flux Φ_s as shown in the figure modulates the Josephson inductance of the SQUID, thus varying the resonance frequency of the SQUID oscillator.

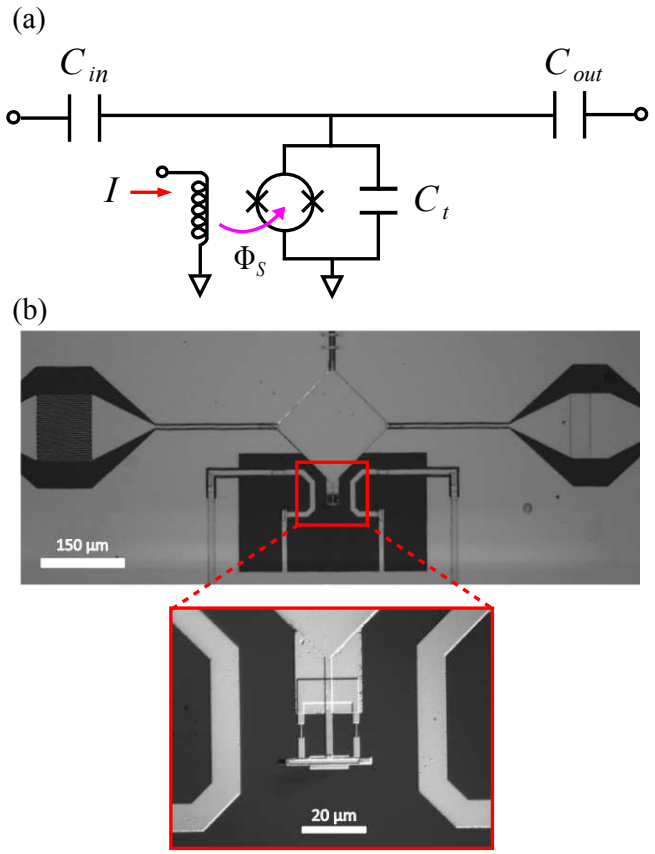

FIG. 1. (Color online) (a) Circuit schematic showing the input/output coupling capacitors and the SQUID oscillator. (b) Optical image of the fabricated circuit with a zoomed-in view of the SQUID with on-chip flux lines.

Our devices are fabricated in a 5-layer process on an oxidized Si wafer. The initial four layers are patterned using photolithography, while the final layer, consisting of the SQUID junctions, is patterned by electron-beam lithography. The ground plane is formed from a 120 nm-thick Al layer. The dielectric layer on top of the ground plane is a 150 nm-thick SiO_2 film deposited by plasma enhanced chemical vapor deposition (PECVD). The SiO_2 forms the dielectric for the parallel plate shunting capacitor C_t and the output coupling capacitor $C_{\rm out}$. The input coupling capacitor $C_{\rm in}$ (Fig. 1) is interdigitated and is formed along with the microwave feedline and the top layer of the parallel plate capacitors in a 200 nm-thick Al film. The estimated value of $C_{\rm in}$, based on the fabricated finger dimensions and using the effective dielectric constant of a microstrip line in the standard expression for the interdigitated capacitor [31, 32], is 0.15 pF. The parallel plate capacitors $C_{\rm out}$ and C_t are designed to be 1.3 pF and 6.8 pF, respectively, based on geometry and film parameters, although there could be significant variation because of our uncertainty in the dielectric proper-

ties of the SiO_2 film. Vias are etched through the SiO_2 layer so that the bias lines and one end of the SQUID contact the ground plane. The SQUID loop is formed so that it is coupled symmetrically between the top and bottom plates of the shunt capacitor [Fig. 1(b)]. The geometric inductanace L_g of the SQUID is calculated to be 43 pH, from FastHenry simulations of the loop dimension ($18 \times 18\,\mu m^2$).

The SQUID junctions are Al-AlO_x-Al, formed by a standard double-angle shadow-evaporation method [33] in a dedicated electron-beam evaporation chamber equipped with *in situ* Ar ion milling to ensure superconducting contacts between the SQUID layer and the junctions. The junctions are sub-micron in size, $530 \times 160\,nm^2$, with a junction capacitance estimated to be 10 fF [34]. The critical current of each junction was estimated to be $0.4\,\mu A$ by measuring the normal state resistance of a nominally identical junction ($684\,\Omega$) and based on our previous characterizations of similar sized junctions [35]. The resonance frequency of the oscillator was designed to be at 3 GHz.

Measurements are performed in a ^{3}He cryostat with a base temperature of 300 mK. A schematic of the measurement setup is shown in Fig. 2(a). A vector network analyzer is used to characterize the resonance frequency, while the transient dynamics are studied using a custom-built GHz DAC (digital to analog converter) and a 20 GHz sampling oscilloscope. The sample chip is wire-bonded to a Cu stripline microwave board and enclosed in an aluminum box for magnetic shielding, which is anchored to the cold plate of the ^{3}He cryostat. The drive-line to the SQUID oscillator is a lossy stainless steel semirigid coaxial cable with attenuators heat sunk at various stages of the cryostat to minimize noise from room temperature. The transmitted signals at the output are amplified by two High Electron Mobility Transistor (HEMT) amplifiers: one at the 4 K stage of the cryostat and another at room temperature with a combined gain of 70 dB. A 6 dB attenuator is used at the output of the oscillator for $50\,\Omega$ impedance matching to the input of the cryogenic HEMT amplifier. The dc biasing lines have copper powder filters anchored at the 1 K stage of the cryostat. A cryogenic μ-metal can surrounds the vacuum can of the cryostat to shield the SQUID from external magnetic fields.

Generation of the microwave pulses is achieved by employing a FPGA based DAC board, which has been built based on the designs from UCSB [36]. A schematic of the pulse generation setup is shown in Fig. 2(b). A nanosecond waveform is generated digitally from the FPGA controlled from a computer. The waveform is passed through Gaussian filters and attenuators before being mixed with a resonant carrier tone at the IQ-mixer, producing a short microwave burst at the output port of the mixer. Different amplitudes of the microwave pulse are achieved by varying the attenuation after the output stage of the mixer with a step attenuator. A typical room temperature trace of the microwave bursts generated by this setup and corresponding time domain measurement is discussed in the next section.

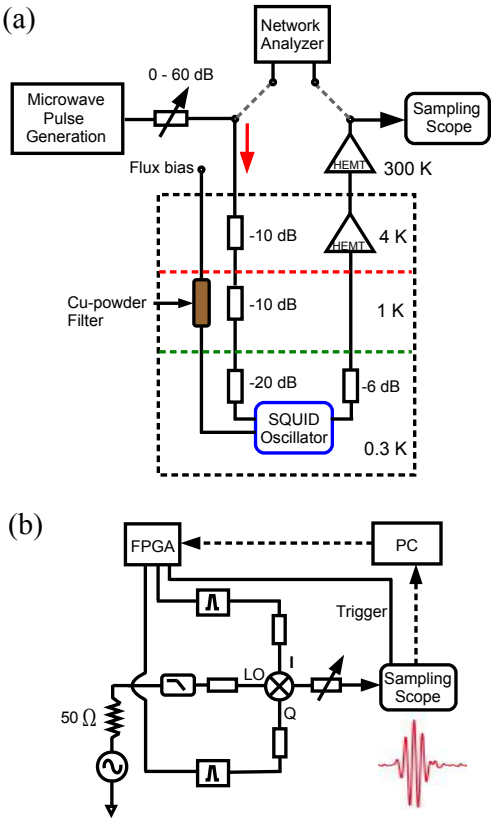

FIG. 2. (Color online) (a) Schematic of general measurement setup. The network analyzer is used to measure the frequency response while the pulse generation setup (expanded in (b)) is used to measure the ringdowns in the time domain. The two types of measurements are separate and, as indicated by dashed lines in (a), the network analyzer is never connected simultaneously with the pulse generation setup. The SQUID oscillator device shown as a blue box is displayed in Fig. 1.

IV. MEASUREMENTS OF THE SQUID OSCILLATOR

The resonance frequency of the SQUID oscillator was characterized as a function of the applied flux at zero bias current ($I_b = 0$). A network analyzer supplied a weak signal with a typical power of -125 dBm to the input of the SQUID oscillator and the 2-port complex transmission parameter, $S_{21}(f)$, was measured. Although, we measured the complex quantity, S_{21}, the plots that we present only show the magnitude, $|S_{21}|$. Multiple $|S_{21}|$ traces were recorded while stepping through the flux applied to the SQUID. Figure 3 shows a density plot of the flux-modulated resonance frequency, periodic in Φ_0, with the color scaling (darker blue) region indicating the highest magnitude of $|S_{21}|$ and the flux axis scaled in units of Φ_0. A phenomenological function of the form

$f(V_{\Phi s}) = \sqrt{a \mid \cos(bV_{\Phi s} + c) \mid}$, where $V_{\Phi s}$ is the flux bias voltage, is used to fit the flux modulation of the resonance peaks over two periods. The fit parameters a, b, c are used to scale the flux axis and fit the frequency values, so that the fit curve (dashed gray line) can be plotted on top of the scaled resonance modulation data, as shown in Fig. 3. The highest frequency at integer Φ_0 occurs at 3.2 GHz. As expected, for $\beta \ll 1$, the critical current, and hence the resonance frequency modulate to near zero. The observed quality factor of the resonance is ~ 7, consistent with the estimated value for the output coupling capacitor and the chip parameters as discussed in the previous Section III. In the following section, we describe a circuit model used to fit the measured $|S_{21}|$ traces as a function of applied flux by calculating the flux-dependent Josephson inductance based on the SQUID potential.

A. Transmission through a SQUID oscillator with asymmetric coupling

A full circuit model is shown in Fig. 5(a), where a Josephson junction, with parallel capacitance C_J, is in series with a geometric inductance $L_g/2$, symmetrically positioned on each side of the SQUID. The external shunt capacitance is labeled as C_t and the internal dissipation in the SQUID oscillator due, for example, to losses in the shunt capacitor, is depicted as R_t. $C_{\rm in}(C_{\rm out})$ is the input (output) coupling capacitor and R_z is the characteristic impedance at the input and output. Neglecting the effects of the small junction capacitances C_J and noting that the dc bias current $I_b = 0$, at low-amplitude drive, such that the Josephson junction is nearly linear, we can describe the SQUID as an effective inductance [37]

$$L_t = \frac{L_{J0}}{2\cos\varphi_-^{\rm min}} + \frac{L_g}{4}. \tag{2}$$

Here $\varphi_-^{\rm min}$ represents the steady state value of φ_-, which for a given value of the applied flux f_s, we can calculate numerically by minimizing the potential energy described by Eq. (1).

Using Eq. (2) we can derive a general expression for S_{21} for the effective parallel LCR tank circuit with asymmetric input and output coupling capacitors. A similar analysis with symmetric coupling capacitors was performed in Ref. [38]. We define $S_{21} = 2V_{\rm out}/V_{\rm in}$ such that a matched load of $R_z = 50\,\Omega$ corresponds to full transmission, $S_{21} = 1$ if the input were connected directly to the output. Then, taking the notation $m \parallel n$ to represent the parallel impedance between impedance elements m and n, we arrive at

$$S_{21}(\omega, L_t) = \frac{2V_{\rm out}}{V_{\rm in}} = 2\frac{R_z}{Z_{\rm out}}\frac{(Z_t \parallel Z_{\rm out})}{(Z_t \parallel Z_{\rm out}) + Z_{\rm in}}, \tag{3}$$

where Z_t is the impedance of the parallel LCR tank circuit,

$$Z_t = \left(\frac{1}{R_t} + \frac{1}{i\omega L_t} + i\omega C_t\right)^{-1} \tag{4}$$

and $Z_{\rm in} = \left(R_z + \frac{1}{i\omega C_{\rm in}}\right)$, $Z_{\rm out} = \left(R_z + \frac{1}{i\omega C_{\rm out}}\right)$ are the input and output impedances respectively.

Equation (3) was used to fit the measured S_{21} traces at each flux bias value. First, the measured S_{21} traces were scaled by the S_{21} transmission at low temperature that was measured on a separate cooldown using a direct coaxial connection in place of the oscillator chip. This scaling of measured S_{21} of the SQUID oscillator resonance by the effective low-temperature baseline takes into account the temperature dependence in the system transmission.

We fit the $S_{21}(f)$ data by fixing $I_0 = 0.4\,\mu$A, $C_{\rm in} = 0.15$ pF and $\beta = 0.05$ and varying C_t and R_t. The estimates for the fixed parameters were explained earlier in Section III. Measured S_{21} curves between $\pm 0.3\,\Phi_0$ were fit simultaneously with the same fixed parameters and the best fit parameters extracted for C_t and R_t were 5.1 pF and 265 Ω respectively. C_t is in reasonable agreement with our estimate based on fabrication parameters described in Section III. We can extract a loss tangent $\tan\delta$ for SiO_2 from the equivalent resistance R_t at a frequency of 2.5 GHz as $1/\omega C_t R_t \sim 4 \times 10^{-2}$. We note that this is roughly an order of magnitude larger than what was measured in Ref. [38] for PECVD-deposited SiO_2 and this difference could be due to variations in deposition conditions and film quality. Also, a precise determination of the internal loss in our capacitor is difficult with these measurements because the large output coupling strength limits the total oscillator quality factor in our circuit. The resonance peaks from the circuit model fits are plotted in Fig. 3 as solid magenta symbols. The extracted fit parameters C_t and R_t are further used in the time-domain simulations described in Section V.

Time-domain measurements were performed by applying a short microwave burst to the SQUID oscillator that was flux biased at $\Phi_s = 0.3\,\Phi_0$, where the resonance frequency, and hence the ringdown waveforms, have high flux sensitivity. An example microwave pulse generated by the GHz DAC is shown in Fig. 4(a) along with the corresponding theoretical fit used for simulations of the ringdowns described in Section V. The voltage signal at the output of the SQUID oscillator is shown in Fig. 4(b) for the case when the SQUID is flux biased at $0.3\,\Phi_0$, corresponding to a resonance frequency of 2.4 GHz. A single experimental ringdown trace shown in the figure is an average of 1000 traces on the sampling oscilloscope. The carrier frequency of the microwave burst is 2.4 GHz, to be on resonance when the SQUID oscillator is biased at $0.3\,\Phi_0$

The SQUID ringdown response to various amplitudes of the drive pulse was mapped out by varying the attenuation on the drive line of the SQUID oscillator. The attenuation was varied in steps of 1 dB from 0 to 40 dB at the top of the cryostat. At a setting of 0 dB, that is, with

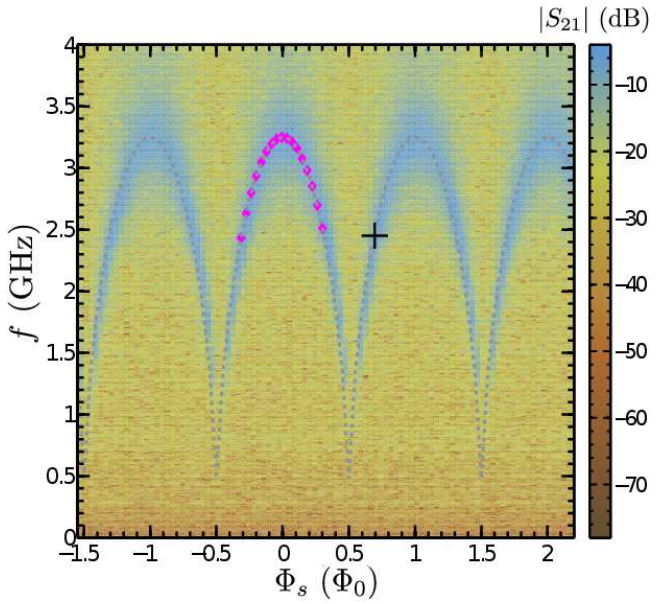

FIG. 3. (Color online) Density plot of $|S_{21}|$ vs. flux and frequency of the SQUID oscillator as measured from a network analyzer at -125 dBm power at the input of the SQUID oscillator chip at 300 mK. The dashed line and magenta symbols are from fits to the SQUID modulation as described in the text. The marker in black indicates the bias point where the pulsed measurements were taken.

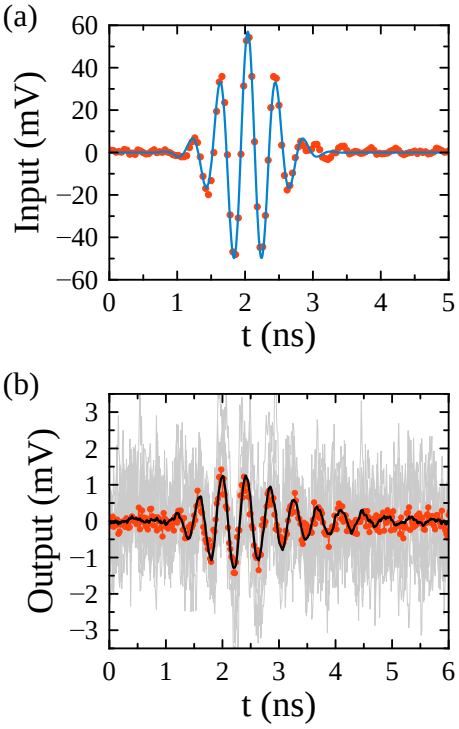

FIG. 4. (Color online) (a) Input pulse as measured at the top of the cryostat. The red dots represent the measured data, while the blue curve is the fit used as the input voltage in the simulations. (b) Example measured output voltage ringdown from the SQUID oscillator. Once again, the red dots were obtained directly from experimental data, while the gray curves in the background are a subset of the realizations obtained from the simulations of the circuit. The average of these realizations is shown in black.

no extra attenuation other than the fixed attenuation inside the cryostat, the measured peak amplitude of the burst at the top of the cryostat was 50 mV. Figure 4(b) displays experimental and theoretical ringdown traces, to be described in more detail in the next section, from the SQUID oscillator when the pulse amplitude driving the SQUID is much smaller than its critical current. The simulated ringdown is shown as a black line while the experimental data is in solid circles.

V. MODEL AND SIMULATIONS

In Sec. IV, where the calibration procedure was described, and where only small drive amplitudes were considered, we treated the Josephson junctions as linear elements, and hence the SQUID as a simple effective inductance. In this section we consider a more complete picture of the full circuit, shown in Fig. 5(a), which accounts for the nonlinearity that is relevant when the applied pulse amplitude is high. In Appendix A we first write down the equations of motion of the full system in terms of five degrees of freedom. Since in our case, the shunt capacitance C_t is much larger than the junction capacitances C_J, and the Josephson inductance of the junctions L_{J0} is in turn much larger than the geometric inductance of the SQUID, L_g (a condition we can write as $\beta = L_g/L_{J0} \ll 1$), we can eliminate the fastest degrees of freedom corresponding to nodes 4 and 5 in Fig. 5(a). Doing so, leaves us with a set of differential equations that govern the behavior of our circuit, of only three degrees of freedom that treat the SQUID potential energy as one-dimensional. Furthermore, in Appendix A, we also discuss how, using the thermodynamic dissipation-fluctuation theorem [39], we can include the effects of noise due to the non-zero temperature of the system. This stochastic noise turns out to play a crucial role in reproducing the experimental behavior when high amplitude input pulses are considered. Combining all of these factors results in the effective equations of motion (in units of current), which can be written using vector notation as

$$\phi_0 \mathbf{C}\ddot{\vec{\varphi}} + \phi_0 \mathbf{R^{-1}}\dot{\vec{\varphi}} + \frac{1}{\phi_0}\vec{\nabla}_\varphi U_{\text{eff}} + \mathbf{N}\vec{n} + \vec{I}_{\text{dr}} = 0. \qquad (5)$$

Here $\vec{\varphi} = (\varphi_1, \varphi_2, \varphi_3)^T$, $\vec{\nabla}_\varphi = (\partial/\partial\varphi_1, \partial/\partial\varphi_2, \partial/\partial\varphi_3)^T$, $\vec{I}_{\text{dr}} = (-V_{\text{in}}/R_z, 0, 0)^T$, $\vec{n} = (n_1, n_2, n_3)^T$ and $\phi_0 = \Phi_0/2\pi$. Each variable φ_i, represents the superconducting phase at node i, with the corresponding voltage defined as $\phi_0\dot{\varphi}_i$. The thermal noise in the circuit is modeled by including a current noise source of strength $\sqrt{\frac{2k_BT}{R_i}}n_i$ in

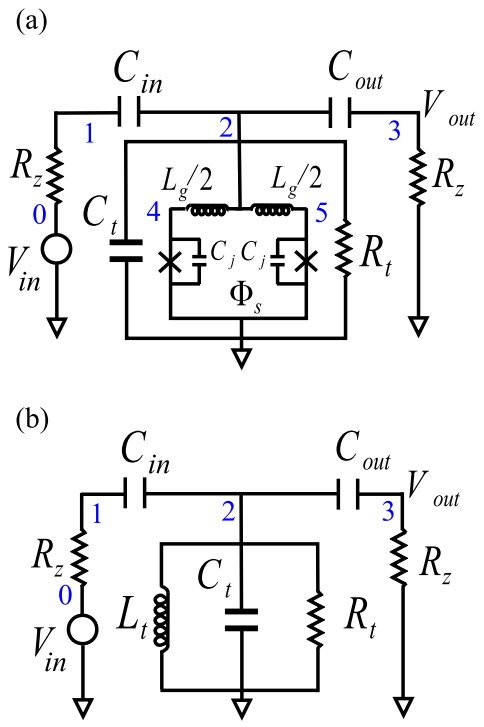

FIG. 5. (Color online) (a) Full circuit model of the SQUID oscillator of Fig. 1 and (b) reduced circuit, valid in the limit of small amplitudes when the Josephson junction responds linearly. In this regime the SQUID is treated as an effective, flux-dependent inductance L_t. In both (a) and (b), the blue numbers represent node labels.

parallel with each resistor R_i. We take k_B to represent the Boltzmann constant, T the temperature and each n_i, a normally distributed random variable, which satisfies

$$\langle n_i(t)\rangle = 0 \tag{6}$$
$$\langle n_i(t)n_j(t')\rangle = \delta(t-t')\delta_{i,j}. \tag{7}$$

In our case, taking $C_\Sigma = C_t + C_{\rm in} + C_{\rm out}$, the matrices corresponding to $\mathbf{C}$ and $\mathbf{R^{-1}}$ can be written as

$$\mathbf{C} = \begin{pmatrix} C_{\rm in} & -C_{\rm in} & 0 \\ -C_{\rm in} & C_\Sigma & -C_{\rm out} \\ 0 & -C_{\rm out} & C_{\rm out} \end{pmatrix}, \mathbf{R^{-1}} = \begin{pmatrix} \frac{1}{R_z} & 0 & 0 \\ 0 & \frac{1}{R_t} & 0 \\ 0 & 0 & \frac{1}{R_z} \end{pmatrix}, \tag{8}$$

and $\mathbf{N}$ as simply

$$\mathbf{N} = \sqrt{2k_BT\mathbf{R^{-1}}}. \tag{9}$$

Finally, $U_{\rm eff}$ represents the effective (drive free) potential energy of our system, which can be decomposed as $U_{\rm eff} = U_0 + U_1$. The terms U_0 and U_1 represent the contributions, up to zeroth and first order in β respectively (as explained in Appendix A), which result in

$$\vec{\nabla}_\varphi U_0 = \begin{pmatrix} 0 \\ 2E_J\cos(\pi f_s)\sin(\varphi_2 + \pi f_s) \\ 0 \end{pmatrix}, \tag{10}$$

$$\vec{\nabla}_\varphi U_1 = \beta \begin{pmatrix} 0 \\ -\frac{E_J}{2}\left(\sin(4\pi f_s + 2\varphi_2) + \sin(2\varphi_2)\right) \\ 0 \end{pmatrix}. \tag{11}$$

Eq. (5) forms a set of stochastic differential equations that we can numerically solve for any φ_i, although each solution only gives us a single realization. Averaging over many such realizations (500 in our case) produces a curve that can be directly compared to the experimental data, which we do in Sec. VI. In our simulations we chose the initial conditions that correspond to the system being at rest, near the potential energy minimum, which we can express as $\dot{\vec{\varphi}}(0) = \vec{0}$ and $\vec{\varphi}(0) = (0, -f_s\pi, 0)^T$ respectively. We then let the system thermalize by evolving Eq. 5 without an external drive present ($\vec{I}_{\rm dr} = \vec{0}$), with only the thermal noise influencing the evolution. In the final step, the input pulse shown in Fig. 4(a) is applied, which in turn excites the system, leading to ringdown oscillations.

A. Model Limitations

In our model, we neglect the internal dissipation associated with each Josephson junction. This is reasonable when the amplitude of the excitation applied to the junctions is smaller than their critical current, as the effective resistance shunting each junction in this case is large enough that its effect on the damping of the junction phase can be neglected. However, in the instances when the driving current exceeds the critical current, each junction experiences a resistance that can be of the order of its normal-state resistance R_n [29], which for the SQUID oscillator studied here is 684 Ω. Nevertheless, in our circuit, the dominant source of noise is the 50 Ω outside load that couples to the SQUID oscillator via $C_{\rm out}$, as can be seen from Fig. 5. When this load is mathematically transformed as impedance parallel with the oscillator over the frequency ranges of the input pulses we apply, its resistive component is never more than 100 Ω, hence a few times smaller than all other sources of noise in the system such that its effect is by far the most dominant.

Furthermore, we neglect any quantum corrections to the noise correlation function and, as is shown in Eq. (7), treat it, just as the rest of the system, fully classically. This is typically a reasonable assumption in the limit of $\hbar\omega \ll 2k_BT$ with ω being the applied, flux dependent, effective natural frequency of the oscillator circuit. In the case of the experimental parameters used here, this limit is largely satisfied, although in the worst case, when the flux through the SQUID is close to integer multiples of a flux quantum (where the effective natural frequency of the oscillator is largest) we are slowly approaching a case where $\hbar\omega \leq 2k_BT$, in particular with $T = 0.300$ K and at $f_s = 0$, we have $\frac{\hbar\omega}{2k_BT} \sim \frac{1}{4}$. Calculating the leading order correction to the quantum version of the correlation

function [40, 41], leads to the following adjusted Eq. (7)

$$\langle n_i(t) n_j(t') \rangle = \left(1 + \frac{1}{48}\right) \delta(t - t') \delta_{i,j}, \qquad (12)$$

which in turn we can interpret as a factor of $\sim 1/24$ change in the amplitude of the noisy current sources associated with each of the resistors. Given that this is the worst case, and this correction gets smaller as the flux that is threaded through the SQUID shifts away from integer multiple of Φ_0, we neglect it in our simulations.

VI. VOLTAGE RINGDOWNS

While we can simulate the evolution of an arbitrary degree of freedom, of particular interest is $\dot{\Phi}_3 = \phi_0 \dot{\varphi}_3$, as it corresponds to the output voltage, which is precisely what is measured in the experiments. As already discussed, we have two "knobs" that can be controlled in a given experimental run; the flux bias f_s, and the amplitude of the input pulse. The rest of the parameters are fixed at the values described in Sec. IV. To explore the behavior of our system better, it is therefore instructive to vary one of these control knobs while keeping the other constant.

A. Amplitude Scans

We first look at amplitude scans, where we fix the applied flux bias f_s and vary the amplitude of the microwave burst, recording a ringdown trace for each excitation strength of the SQUID oscillator. Figure 6 displays density plots of such a case, obtained with experimental data (top plot) and from simulations (bottom plot). The flux f_s is fixed at 0.30, which corresponds to the natural frequency of the SQUID of 2.4 GHz (when the SQUID is operated in a linear regime), satisfying a resonance condition. The y-axis, is the attenuation setting from the highest (40 dB) to the lowest attenuation (0 dB) corresponding to increasing burst amplitude towards the bottom of the plot and the x-axis is the ringdown time in nanoseconds. The color scale indicates the amplitude of the ringdown. With increasing pulse strength, the frequency of the ringdowns decreases. This becomes particularly pronounced for attenuation levels less than 20 dB. This shift to lower frequencies arises because the fictitious particle, whose position coordinate can be described by the ϕ_2 degree of freedom, begins to explore the nonlinear (flatter) part of the potential energy landscape. For attenuation levels less than 12 dB, we observe a sharp drop in the resulting ringdowns. At this point, the strength of the drive is now of the order of the critical current of the SQUID. The stochastic nature of the thermal noise causes different realizations to escape the potential well at different times, which in turn causes a substantial decay in the ringdown signal strength. This phenomenon is discussed in more detail in the next section.

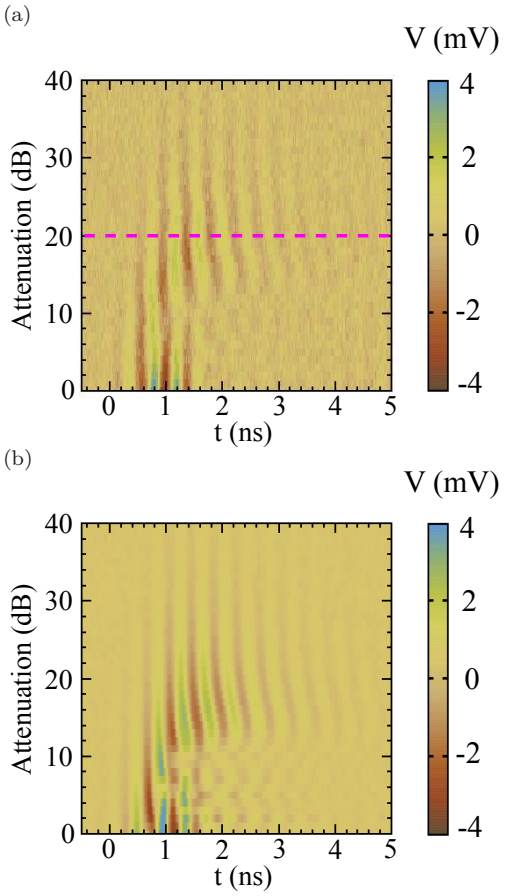

FIG. 6. (Color online) A comparison of the amplitude dependence of ringdowns at a non-integer flux bias of $f_s = 0.30$, for the input signal of Fig. 4(a) at 2.4 GHz. The plot in (a) shows experimental data, while in (b), the corresponding simulations. The attenuation on the drive pulse in dB is shown on the y-axis, with decreasing numbers implying increasing amplitude of the input pulse. The ringdown time is shown on the x-axis while the ringdown amplitude is represented by the color scale. The purple dashed line in (a) indicates the amplitude corresponding to the ringdown trace shown in Fig. 4(b).

B. Escape from the Potential Well

The problem of particle escape from a potential well due to thermal noise has been investigated both theoretically as well as experimentally in a variety of studies [42–46]. In the case of a dc SQUID, this rate can be approximated to be proportional to $\Omega \exp(-U_b/k_B T)$ where U_b represents the potential energy barrier height that the particle has to overcome, and Ω the natural frequency along the direction of escape. In our case, since we do not "tilt" the potential with a dc bias current, the escape time (inverse rate) can be shown to be much larger than the typical experimental run time. This is true over almost all settings of the applied flux bias f_s, except when $f_s \simeq 0.50$, where the potential barrier is close to being flat.

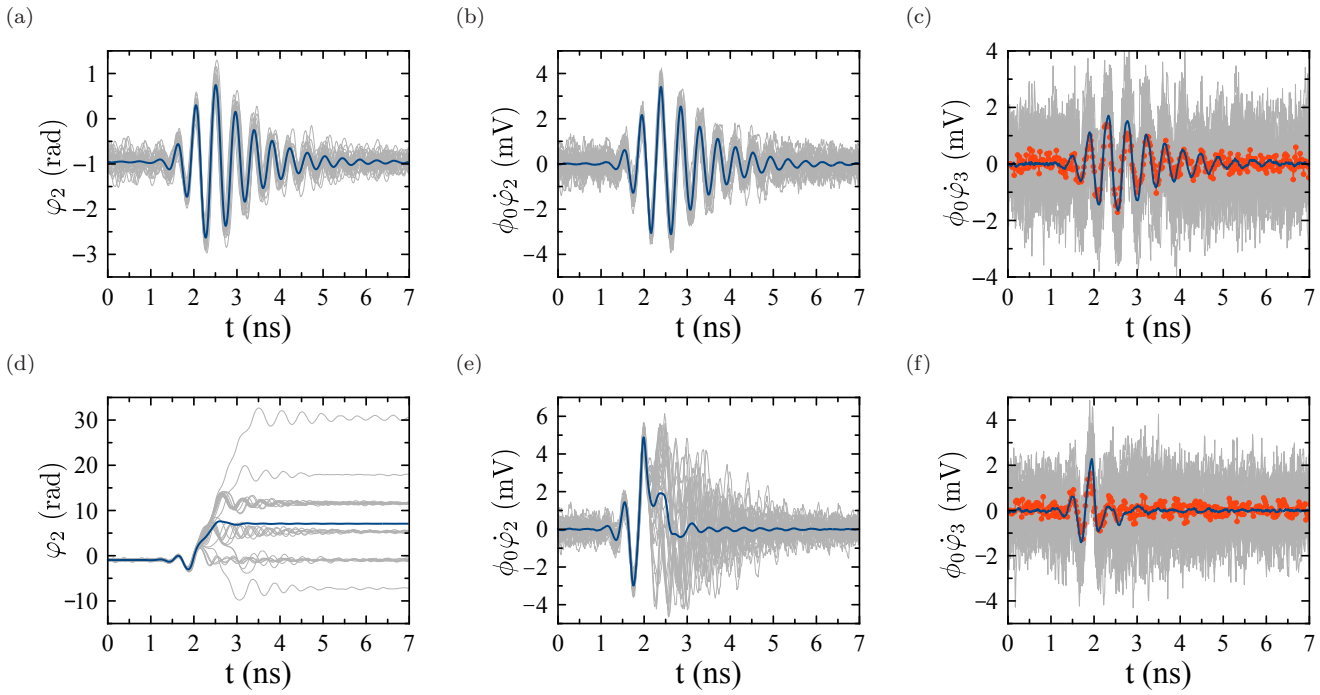

FIG. 7. (Color online) Low and high drive response. Each row shows plots of $\varphi_2(t)$, $\phi_0\dot{\varphi}_2(t)$ and $\phi_0\dot{\varphi}_3(t)$ (the output voltage) respectively. In plots (a-c), the amplitude of the input pulse is low with respect to the critical current of the Josephson junctions, whereas in (d-f) it is high. The gray curves show a small subset of individual realizations used to calculate the averages (blue curves). In the case of the third column we also show the experimental data for the same parameters (red dots) and how it compares to the simulation results. From the plots, one clearly sees how when the drive is low, all the realizations stay within the same potential well (see plot a), and their relative phase shift only varies slightly. In the case of high drive, we observe that different realizations tend to end up in different wells at different times (as shown in plot d), which introduces a relative phase shift between them. This in turn leads to faster decay of the average voltage, which is reflected in plots (e) and (f).

Thermal fluctuations, however, still end up playing an important role in the evolution of the system. In particular, we find that during strong pulses that excite the system to amplitudes in the vicinity of the SQUID's critical current, the thermal fluctuations can cause a strong mixing in the phases of various realizations, resulting in a damping of the ringdowns. To our knowledge, no detailed analytical study of this effect, with strongly time-dependent, transient pulses has been performed yet, but we can still study the situation numerically. To do this, we once again fix the applied flux bias at $f_s = 0.30$ as in the previous section, and concentrate on two different pulses: the first at an attenuation of 15 dB and the other at the attenuation of 10 dB. From Fig. 6, we can see that these correspond to cases where substantial ringdown voltage is observed (the former case) and where the ringdowns are dramatically suppressed (the latter case).

In order to understand this behavior in more detail, we look at the evolution of the individual realizations, that so far have been averaged to obtain results comparable with the experiment. We stress, however, that while the behavior of the full circuit is largely governed by the dynamics of the SQUID, the experiment only provides us access to the external voltage — the voltage at node 3 in Fig. 5 — which in our simulations is represented mathematically as $\phi_0\dot{\varphi}_3$. To directly observe the stochastic nature of the escape from the potential well, we need to look at the individual realizations of the full system. Of particular interest are the following simulation variables: φ_2, which represents the phase (i.e., the effective "position") of the SQUID degree of freedom, that dominates the evolution of the system, $\phi_0\dot{\varphi}_2$, which represents the voltage across the SQUID (or alternatively an effective "velocity" of the particle in the well), and finally $\phi_0\dot{\varphi}_3$, which is the voltage that we can directly compare to the experimental data. Figure 7 shows plots that describe the evolution of these variables as a function of time. The top row shows data for a case of the low amplitude, 15 dB attenuation pulse, while the bottom row shows the case of high amplitude, 10 dB attenuation pulse. The leftmost column represents $\varphi_2(t)$, the middle column $\phi_0\dot{\varphi}_2(t)$, and finally the rightmost column is the output voltage, namely $\phi_0\dot{\varphi}_3(t)$. In each case, the grey curves represent a subset of realizations that are averaged (curves in blue). The red dots in the plots from the rightmost column represent experimental data for the same set of parameters as the simulations. The key signature of the escape can be seen in the leftmost column. Here, when the pulse amplitude

is low (top row), virtually all the realizations stay within the same potential well — as one can see by noting that they all oscillate around the same value of φ_2, namely $\varphi_2 \sim -0.30\pi$. In the case of the high amplitude pulse (bottom row), different realizations jump out to different potential wells. The stochastic nature of the noise causes these jumps to happen at different times, which leads to a randomly shifted phase, as well as a different steady state value of φ_2. This has a substantial effect on the "velocity" (or $\dot{\varphi}_2$) of these realizations, as shown in the central column of Fig. 7. The result is a dramatic randomization in the phase of $\dot{\varphi}_2$, and as a result, of $\dot{\varphi}_3$, which is proportional to the output voltage of the circuit. As we see from the experimental voltage (red dots), the agreement of the measured data with the simulations is good. Finally, we stress that including the stochastic effects of thermal noise in our simulations has been crucial in reproducing this behavior.

C. Flux Scans

We explore the voltage ringdown behavior further by studying their dependence on the magnetic flux applied to the SQUID. Here, the amplitude and frequency of the microwave burst is fixed while we vary the flux applied to the SQUID through one period of a flux quantum. The pulse frequency once again is chosen to correspond to resonance at the SQUID flux bias $f_s \sim 0.30$. The density plots of the flux-modulated ringdown traces is shown in Fig. 8 for three different pulse amplitudes. The top row shows plots obtained from experimental data, while the bottom row shows the simulations. The leftmost column has a low input pulse amplitude with 20 dB of attenuation, well below the critical current of the SQUID, the central column shows data for an input pulse with 15 dB of attenuation, while the rightmost column has a high amplitude pulse with 10 dB of attenuation. By varying the applied flux through the SQUID, we are changing its effective inductance, and hence its natural frequency. It is worth stressing that this nonlinear dependence of the natural frequency on the applied flux is true even in the limit of small oscillations of the SQUID (where $|\varphi_2| \ll 1$), as was already discussed in Sec. IV. Let us first concentrate on the leftmost column of Fig. 8. Here the drive amplitude is still small and the nonlinearity of the potential energy in φ_2 is only beginning to play a role. Yet, as the applied flux bias f_s varies between 0 and 1, the ringdowns tend to fan out. As expected, the amplitude is largest near the flux bias of $f_s \sim 0.30$, since this is where the SQUID is resonant with the input pulse, and it is suppressed elsewhere. The results are also consistent with the fact that the natural frequency, up to zeroth order in β, is proportional to $\sqrt{\cos(\pi f_s)}$. Hence, near $f_s \sim 0$, the variations in the ringdown structure are small, while at the same time, one sees a very abrupt suppression near $f_s \sim 0.50$. Here the effective natural frequency of the SQUID is very small and the short input pulse is unable to induce strong oscillations. This is an adiabatic regime, where the excitation of the circuit strongly follows the input pulse. In this regime, the ringdown suppression due to a highly off-resonant pulse can be confirmed further by studying individual realizations and showing that they stay in the same potential energy well as they started in, in contrast to what is observed during an escape — see Sec. VI B. Furthermore, a very similar ringdown structure can be obtained in a case where a simple harmonic oscillator, with the same flux-dependent form of natural frequency, is driven with the same pulse waveform. The situation is largely similar in the middle column of Fig. 8. The key difference here is that now, not only is the natural frequency of the system nonlinear in the applied flux, but the amplitude of the input pulse is large enough for the SQUID degree of freedom φ_2 to start exploring the nonlinear regions of the potential energy well. This effect is particularly strong around the applied flux bias for which the SQUID is resonant with the input pulse (near $f_s \sim 0.30$). This in turn affects the degree of variation of the ringdown frequency with respect to f_s, as can be seen in the plots. Finally, in the rightmost column we see a case of a strongly driven system. The resulting plots show an overall suppression of ringdown oscillations across all values of f_s, when compared to the instances with smaller drive amplitudes. In this case, the reason is two-fold. By once again studying the individual realizations as in Sec. VI B, we can conclude that for the applied flux away from $f_s = 0.50$, the main culprit in the suppression is the randomization of the phase of φ_2 due to the stochastic escape from the potential well. Near $f_s = 0.50$ however, as in the case of low amplitude pulses, the main reason for the suppression is the off-resonance condition, where the frequency of the pulse is much greater that the natural frequency of the SQUID.

VII. APPLICATION TO FLUX MEASUREMENTS

The high sensitivity of SQUIDs to applied flux has made them exquisite detectors of flux signals. They have been useful in various metrology experiments [9, 47–50] and more recently have played an important role in the field of quantum computing, as measurement devices for flux qubits [10–13, 51]. In these applications, a flux qubit is typically coupled inductively to a SQUID and hence affects the net applied flux that is threaded through the device. One of the original SQUID-based readout approaches involves biasing the SQUID with an appropriately selected dc current, such that the SQUID is put in a running state with non-zero voltage, with a high probability if the qubit is in one state, and with negligible probability when the qubit is in the other state [7]. In an alternate approach, the SQUID is driven with a continuous sinusoidal signal while monitoring the resulting phase shift, which is qubit-state dependent [52]. Yet

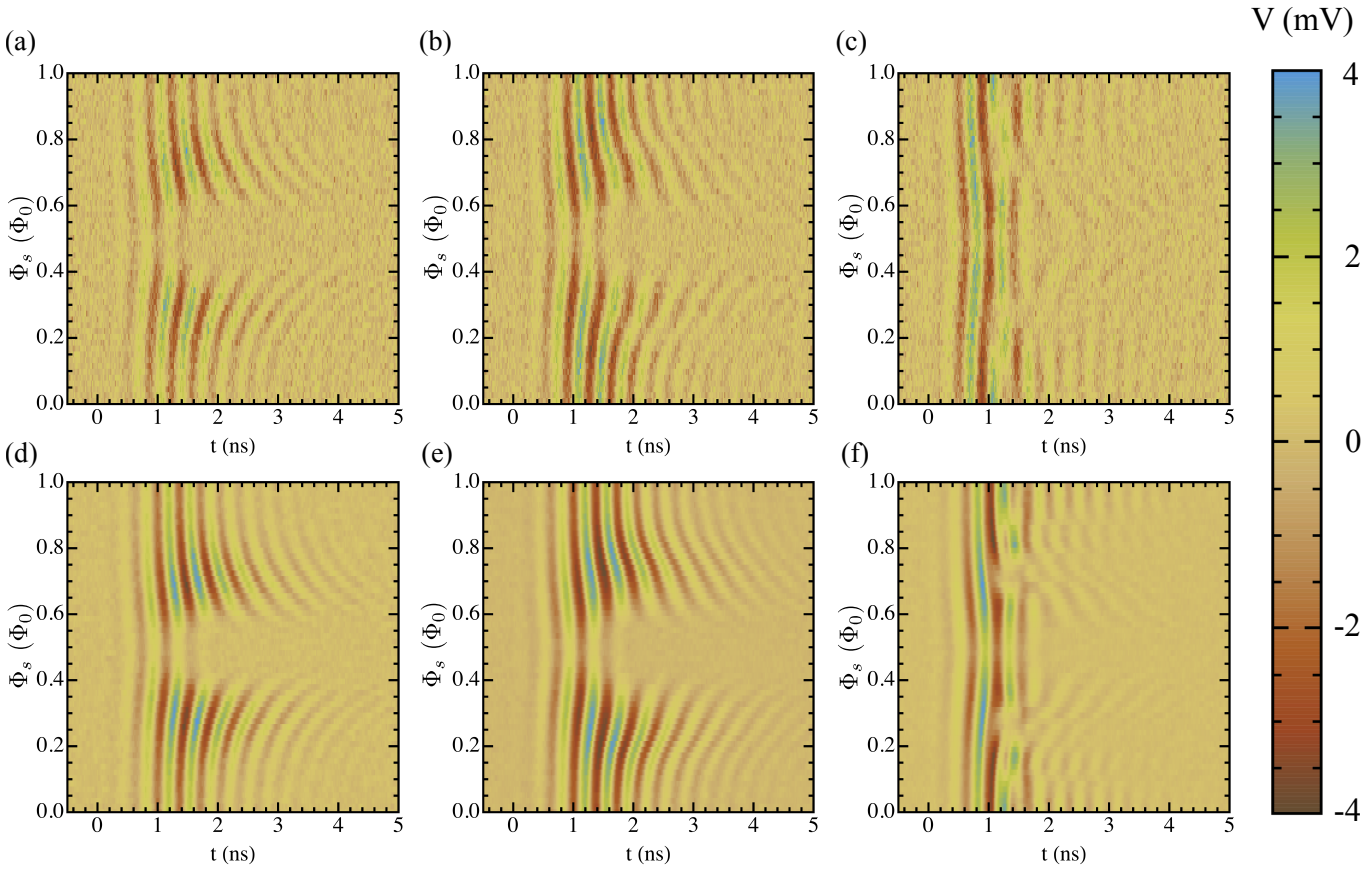

FIG. 8. (Color online) Fixed amplitude flux scans with the applied flux bias f_s between 0 and 1, and with the input signal of Fig. 4(a) at 2.4GHz. The top row (a-c) shows experimental data, while the bottom row (d-f), uses data obtained by running stochastic simulations. The amplitude of the input pulse increases from left to right, with the leftmost column showing results for 20 dB attenuation pulses, the middle column for 15 dB attenuation pulses, and finally the rightmost column for 10 dB attenuation pulses. As the amplitude increases, one clearly observes the effects of the nonlinearity of the system. See main text for a more detailed discussion.

another proposed readout scheme uses brief, but strong, current bias pulses to the SQUID, which result in ringdown dynamics with an amplitude, and possibly phase, that depend on the qubit state [53]. This is somewhat analogous to what is presented in the experiment described here, although clearly in our case the flux differences are due to a global flux biasing as no qubit is actually present. Furthermore, the theoretical proposal outlined in [53] shows a full quantum treatment of the qubit and SQUID system, but only considers an ultrashort dc pulse, much shorter than the inverse characteristic qubit frequency. Due to the relatively high temperature of our measurements, our present experiment is in the classical regime, and involves input pulses with a time scale comparable to the dynamics of the circuit. Nevertheless, it is still useful to explore briefly just how the process of discrimination between two or more different flux states could be accomplished with our system. First, one can expect that the total applied flux through the SQUID would consist of some static bias flux $\Phi_{\rm bias}$ plus a signal flux that is to be measured, say $\Phi_{\rm signal}$. One could then send a microwave pulse through the SQUID, analogous to what was considered here, and record the corresponding ringdown voltage. Some post-processing of this ringdown voltage, such as, for example, taking its root-mean-squared value, $V_{\rm rms}$, integrated over a suitably chosen time range, would provide a level corresponding to the signal flux. As long as these levels of various values of $\Phi_{\rm signal}$ can be distinguished, one has an effective flux meter. For a given input pulse, assuming that $V_{\rm rms}$ is a well behaved function of the total SQUID flux Φ_s, one possible way to find the best $\Phi_{\rm bias}$ over a range of flux where $V_{\rm rms}$ is monotonic would be simply to look for the largest slope of $V_{\rm rms}$ with respect to Φ_s, namely maximizing $\partial V_{\rm rms}(t_{\rm int}, \Phi_s)/\partial \Phi_s$ over all possible flux Φ_s between 0 and $0.5\Phi_0$ (due to symmetry) and integration times $t_{\rm int}$. This would give the greatest contrast between the cases of $\Phi_{\rm bias} + \Phi_{\rm signal}$ and $\Phi_{\rm bias} - \Phi_{\rm signal}$. Figure 9 shows an explicit example of this kind of flux discrimination based on our measurements, where we calculate $V_{\rm rms}$ over a time range between 2.1 and 3.4 ns. The data that is being used corresponds to the input signal with 20 dB attenuation, and is the same as in the flux-scans from Fig. 8. The dots represent results obtained from

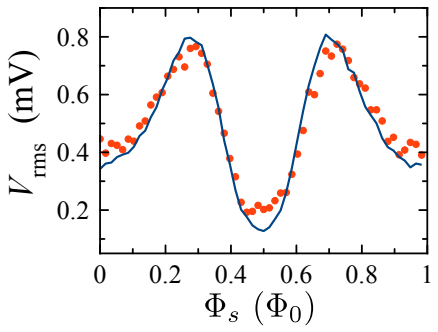

FIG. 9. (Color online) Root mean square output voltage $V_{\rm rms}$ as a function of the applied flux bias Φ_s, calculated over a time range between 2.1 and 3.4 ns. The plot uses data obtained with the 20 dB attenuation input pulses, and is the same as in the left column of the flux-scans from Fig. 8. The dots represent results calculated from the experimental data (top row, leftmost column), while the solid line is produced using the simulations (bottom row, leftmost column). By biasing the flux through the SQUID near a point where the slope is high, for example at $\Phi_s \sim 0.36\Phi_0$, one can have a means of distinguishing between different flux signals — see main text for more details.

the experimental data (top row, leftmost column), while the solid line is produced from the evolution calculated through stochastic simulations (bottom row, leftmost column). We can further make a crude calculation of the required sensitivity that one would need with the data from Fig. 9 to distinguish between two hypothetical flux qubit states. Setting the bias flux at $\Phi_{\rm bias} \sim 0.36\Phi_0$ the slope is roughly $5\,{\rm mV}/\Phi_0$. If we assume a conservative noise temperature of 150 mK for a ~ 3 GHz amplifier with a bandwidth of 100 MHz [54, 55], the rms voltage noise at the amplifier input would be ~ 200 nV. If we take the $5\,{\rm mV}/\Phi_0$ slope for the signal at the output extracted from Fig. 9, and divide by the net gain of the HEMT amplifiers (~ 55 dB), this becomes $9\,\mu{\rm V}/\Phi_0$ at the SQUID oscillator output. We consider a peak-to-peak qubit flux signal of $22\,{\rm m}\Phi_0$, which is reasonable[7, 56, 57], considering the back-action on the qubit would also likely be significantly less compared to a switching dc SQUID measurement, since the SQUID never enters the running state. This then corresponds to a SNR of ~ 1. So, we would be right at the threshold for reading out the ringdowns and distinguishing between the two qubit states in a single shot. We should further stress that one could likely do better by both using more sensitive amplifiers and optimizing various parameters. Of particular importance would be integration time $t_{\rm int}$, the pulse amplitude, as well as the quality factor of the SQUID oscillator, all of which the $V_{\rm rms}$ curves are highly dependent on.

VIII. CONCLUSIONS

In conclusion, we have studied the transient behavior of a dc SQUID operated as a nonlinear oscillator under pulsed ac excitation. Both experimentally as well as numerically, we applied signals of various amplitudes for different flux bias, while observing the resulting voltage ringdowns. In order to account for the non-zero temperature of the experiment, we used the Johnson-Nyquist approach and modeled resistors as noisy current sources. This let us numerically reproduce the stochastic escape dynamics observed when the SQUID was driven with high-amplitude pulses. Finally, we briefly discussed the potential applicability of our system, and in particular the observed ringdown dynamics, to flux measurement. We found a good general agreement between the experimental data and results obtained through numerical simulations.

IX. ACKNOWLEDGMENTS

This work was supported by the DARPA/MTO QuEST program through a grant from AFOSR. PG and FKW acknowledge support by NSERC and FKW also support by the European union through SCALEQIT. Device fabrication was performed at the Cornell NanoScale Facility, a member of the National Nanotechnology Infrastructure Network, which is supported by the National Science Foundation (Grant ECCS-0335765). PG would like to thank Chunqing Deng for a useful discussion on the Born-Oppenheimer approximation, and Anthony J. Leggett for his helpful remarks regarding the applicability of our model.

Appendix A: Equations Of Motion

In this section we present a derivation of the equations of motion of a circuit which was used to model our experimental apparatus. We start with a full description of the system at zero-temperature and reduce the equations of motion by eliminating fast degrees of freedom. We then add the effects of the temperature-dependent noise.

1. Zero Temperature

As discussed in Section III above, the circuit diagram is shown in Fig. 5. Our model assumes that the external flux is delivered directly to the SQUID loop, and other branches have no intrinsic geometric inductance. We further neglect the mutual inductance in the system other than the one that mediates the external flux Φ_s. To obtain the equations of motion, we follow the treatment of Devoret [58]. With each node i, we associate a

corresponding node flux Φ_i related to a node voltage by $\Phi_i = \int_{-\infty}^{t} dt' V(t')$. We express the currents across elements in terms of Φ_i and using Kirchoff's current conservation conditions at each node i, arrive at the equations of motion

$$\begin{aligned}
\frac{1}{R_z}(V_{\rm in} - \dot{\Phi}_1) =& C_{\rm in}(\ddot{\Phi}_1 - \ddot{\Phi}_2) \\
C_{\rm in}(\ddot{\Phi}_1 - \ddot{\Phi}_2) =& \frac{2}{L_g}(\Phi_2 - \Phi_4 + \Phi_s) + \frac{2}{L_g}(\Phi_2 - \Phi_5) \\
&+ C_t\ddot{\Phi}_2 + \frac{1}{R_t}\dot{\Phi}_2 + C_{\rm out}(\ddot{\Phi}_2 - \ddot{\Phi}_3) \\
C_{\rm out}(\ddot{\Phi}_2 - \ddot{\Phi}_3) =& \frac{1}{R_z}\dot{\Phi}_3 \\
\frac{2}{L_g}(\Phi_2 - \Phi_4 + \Phi_s) =& I_0 \sin(\Phi_4 2\pi/\Phi_0) + \frac{1}{R_i}\dot{\Phi}_4 + C_J\ddot{\Phi}_4 \\
\frac{2}{L_g}(\Phi_2 - \Phi_5) =& I_0 \sin(\Phi_5 2\pi/\Phi_0) + \frac{1}{R_i}\dot{\Phi}_5 + C_J\ddot{\Phi}_5
\end{aligned}$$

Next, taking the flux quantum $\Phi_0 = 2.07 \times 10^{-15}$Wb $= 2\pi\phi_0$, we perform a change of variables so that $\Phi_i = \frac{\Phi_0}{2\pi}\varphi_i = \phi_0\varphi_i$. Here, a difference $\varphi_i - \varphi_j$ for some $i \neq j$, corresponds to the superconducting phase difference. We further take $\varphi_\pm = \frac{1}{2}(\varphi_4 \pm \varphi_5)$, $C_\Sigma = C_{\rm in} + C_{\rm out} + C_t$, $L_{J0} = \Phi_0/2\pi I_0$ and rewrite the external flux Φ_s in terms of the ratio $f_s = \frac{\Phi_s}{\Phi_0}$. After dividing all equations by ϕ_0, we have

$$\begin{aligned}
0 =& C_{\rm in}\ddot{\varphi}_1 - C_{\rm in}\ddot{\varphi}_2 + \frac{1}{R_z}\dot{\varphi}_1 - \frac{1}{\phi_0 R_z}V_{\rm in} \\
0 =& -C_{\rm in}\ddot{\varphi}_1 + C_\Sigma\ddot{\varphi}_2 - C_{\rm out}\ddot{\varphi}_3 + \frac{1}{R_t}\dot{\varphi}_2 \\
&+ \frac{4}{L_g}(\varphi_2 - \varphi_+ + \pi f_s) \\
0 =& -C_{\rm out}\ddot{\varphi}_2 + C_{\rm out}\ddot{\varphi}_3 + \frac{1}{R_z}\dot{\varphi}_3 \\
0 =& 2C_J\ddot{\varphi}_+ + \frac{2}{L_{J0}}\sin\varphi_+\cos\varphi_- - \frac{4}{L_g}(\varphi_2 - \varphi_+ + \pi f_s) \\
0 =& 2C_J\ddot{\varphi}_- + \frac{2}{L_{J0}}\sin\varphi_-\cos\varphi_+ - \frac{4}{L_g}(-\varphi_- + \pi f_s).
\end{aligned}$$

Thus, we end up with equations of motion for five degrees of freedom. In order to further simplify the above, we note that in our case, the capacitances (or effective masses) of oscillators φ_+ and φ_- are two orders of magnitude smaller than that of φ_2. Furthermore, the Josephson inductance L_{J0} is much greater than the geometric inductance L_g. This allows us to apply an Oppenheimer-Born-like approximation and eliminate the fast-oscillating degrees of freedom φ_+ and φ_-. To do this, we first define a potential energy U that can be associated with our system. Neglecting terms due to the external drive, we have

$$\begin{aligned}
\frac{U}{2E_J} =& -\cos\varphi_+\cos\varphi_- + \frac{1}{\beta}(\varphi_- - \pi f_s)^2 \\
&+ \frac{1}{\beta}(\varphi_+ - (\varphi_2 + \pi f_s))^2,
\end{aligned} \tag{A1}$$

with $\beta = L_g/L_{J0}$. Next, we fix the slow variable φ_2, and note that since $\beta \ll 1$, the second and third terms in Eq. (A1) will dominate. Hence the minima of U will be close to $\varphi_+ = \varphi_2 + \pi f_s$ and $\varphi_- = \pi f_s$. By expanding U near these points and minimizing, we can calculate the corrections to the minimum points. Keeping terms up to first order in β we arrive at

$$\varphi_-^{\rm min} = \pi f_s - \beta\frac{\sin(\pi f_s)\cos(\pi f_s + \varphi_2)}{2} \tag{A2}$$

$$\varphi_+^{\rm min} = \pi f_s + \varphi_2 - \beta\frac{\cos(\pi f_s)\sin(\pi f_s + \varphi_2)}{2}. \tag{A3}$$

These results are then substituted back into the expanded potential energy, which leads to $U_{\rm eff} = U_0 + U_1$, now only in terms of φ_2 and with

$$\frac{U_0}{2E_J} = -\cos(\pi f_s)\cos(\varphi_2 + \pi f_s)$$

and

$$\begin{aligned}
\frac{U_1}{2E_J} =& -\frac{\beta}{2}\left(\sin^2(\pi f_s)\cos^2(\pi f_s + \varphi_2)\right. \\
&\left. + \cos^2(\pi f_s)\sin^2(\pi f_s + \varphi_2)\right).
\end{aligned} \tag{A4}$$

We have distinguished between the contributions to the effective potential energy between terms of different orders in β. U_0 neglects the geometric inductance completely, while U_1 shows the correction up to first order in β. We can hence write a set of effective equations of motion with $U_{\rm eff}$ as the potential energy, while now including drive term, as

$$0 = C_{\rm in}\ddot{\varphi}_1 - C_{\rm in}\ddot{\varphi}_2 + \frac{1}{R_z}\dot{\varphi}_1 - \frac{1}{\phi_0 R_z}V_{\rm in} \tag{A5}$$

$$\begin{aligned}
0 =& -C_{\rm in}\ddot{\varphi}_1 + C_\Sigma\ddot{\varphi}_2 - C_{\rm out}\ddot{\varphi}_3 + \frac{1}{R_t}\dot{\varphi}_2 \\
&+ \frac{2}{L_{J0}}\cos(\pi f_s)\sin(\varphi_2 + \pi f_s) \\
&- \beta\left(\frac{\sin(4\pi f_s + 2\varphi_2) + \sin(2\varphi_2)}{2L_{J0}}\right)
\end{aligned} \tag{A6}$$

$$0 = -C_{\rm out}\ddot{\varphi}_2 + C_{\rm out}\ddot{\varphi}_3 + \frac{1}{R_z}\dot{\varphi}_3. \tag{A7}$$

The next step is to account for the non-zero temperature of the system.

2. Non-zero Temperature

We find that the accounting for thermal noise is of particular importance when comparing with the behavior of the experimental system in our simulations, in particular at high amplitude pulses. In order to model these effects, we use the thermodynamic dissipation-fluctuation relation [39]. Thermal noise in the circuit is modeled by including a current noise source of strength $\sqrt{\frac{2k_BT}{R_i}}n_i$ in

parallel with each resistor R_i. We take k_B as the Boltzman constant, and T the temperature of the system. Furthermore, each $n_i(t)$ represents a normally distributed random variable, namely $n_i \in \mathcal{N}(0,1)$, that satisfies the following

$$\langle n_i(t)\rangle = 0 \tag{A8}$$
$$\langle n_i(t) n_j(t')\rangle = \delta(t-t')\delta_{i,j}. \tag{A9}$$

Adding such a noisy current in parallel with each of the resistors to the effective model derived in Sec. A 1 leads to classical Langevin equations, which after rearranging, can be written in a vector form as Eq. (5).

[1] A. J. Leggett, Testing the limits of quantum mechanics: motivation, state of play, prospects, J. Phys.: Condens. Matter **14**, R415 (2002).

[2] J. Clarke and F. K Wilhelm, Superconducting quantum bits, Nature **453**, 1031 (2008).

[3] M. H. Devoret, J. M. Martinis, and J. Clarke, Measurements of Macroscopic Quantum Tunneling out of the Zero-Voltage State of a Current-Biased Josephson Junction, Physical Review Letters **55**, 1908 (1985).

[4] F. Balestro, J. Claudon, J. P. Pekola, and O. Buisson, Evidence of two-dimensional macroscopic quantum tunneling of a current-biased dc SQUID, Physical Review Letters **91**, 158301 (2003).

[5] J. M. Martinis, M. H. Devoret, and J. Clarke, Energy-Level Quantization in the Zero-Voltage State of a Current-Biased Josephson Junction, Physical Review Letters **55**, 1543 (1985).

[6] Y. Y. Nakamura, C. D. Chen, and J. S. Tsai, Spectroscopy of Energy-Level Splitting between Two Macroscopic Quantum States of Charge Coherently Superposed by Josephson Coupling, Physical Review Letters **79**, 2328 (1997).

[7] C. H. van der Wal, F. K. ter Haar, A. C. J.and Wilhelm, R. N. Schouten, C. J. P. M. Harmans, T. P. Orlando, S Lloyd, and J. E. Mooij, Quantum Superposition of Macroscopic Persistent-Current States, Science **290**, 773 (2000).

[8] J.M. Martinis, S. Nam, J. Aumentado, and C. Urbina, Rabi oscillations in a large Josephson-junction qubit, Physical Review Letters **89**, 117901 (2002).

[9] J. Clarke and A. I. Braginski, *The SQUID Handbook: Fundamentals and Technology of SQUIDs and SQUID Systems Vol. I* (Wiley, Weinheim, 2004).

[10] I. Chiorescu, P. Bertet, K. Semba, Y. Nakamura, C. J. P. M. Harmans, and J. E. J. E. Mooij, Coherent dynamics of a flux qubit coupled to a harmonic oscillator, Nature **431**, 159 (2004).

[11] A. Lupascu, S. Saito, T. Picot, P. C. De Groot, C. J. P. M. Harmans, and J. E. Mooij, Quantum non-demolition measurement of a superconducting two-level system, Nature Physics **3**, 119 (2007).

[12] D. Vion, A. Aassime, A. Cottet, P. Joyez, H. Pothier, C. Urbina, D. Esteve, and M. H. Devoret, Manipulating the Quantum State of an Electrical Circuit, Science **296**, 886 (2002).

[13] J. Claudon, A. Fay, E. Hoskinson, and O. Buisson, Nanosecond quantum state detection in a current-biased dc SQUID, Phys. Rev. B **76**, 024508 (2007).

[14] I. Siddiqi, R. Vijay, F. Pierre, C. M. Wilson, L. Frunzio, M. Metcalfe, C. Rigetti, R. J. Schoelkopf, M. H. Devoret, D. Vion, and D. Esteve, Direct Observation of Dynamical Bifurcation between Two Driven Oscillation States of a Josephson Junction, Physical Review Letters **94**, 027005 (2005).

[15] R. Vijay, M. H. Devoret, and I. Siddiqi, Invited Review Article: The Josephson bifurcation amplifier, Rev. Sci. Instrum. **80**, 111101 (2009).

[16] Michael Mück and Robert McDermott, Radio-frequency amplifiers based on dc squids, Supercon. Sci. Technol. **23**, 093001 (2010).

[17] D. Hover, Y.-F. Chen, G.J. Ribelli, S. Zhu, S. Sendelbach, and R. McDermott, Superconducting low-inductance undulatory galvanometer microwave amplifier, Appl. Phys. Lett. **10**, 063503 (2012).

[18] B. Yurke, L.R. Corruccini, P.G. Kaminsky, L.W. Rupp, A.D. Smith, A.H. Silver, R.W. Simon, and E.A. Whittacker, Observation of parametric amplification and deamplification in a josephson parametric amplifier, Phys. Rev. A **39**, 2519 (1989).

[19] M.A. Castellanos-Beltran, K.D. Irwin, G.C. Hilton, L.R. Vale, and K.W. Lehnert, Amplification and squeezing of quantum noise with a tunable josephson metamaterial, Nat. Phys. **4**, 929 (2008).

[20] M. Hatridge, R. Vijay, D.H. Slichter, J. Clarke, and I. Siddiqi, Dispersive magnetometry with a quantum limited squid parametric amplifier, Phys. Rev. B **83**, 134501 (2011).

[21] N. Bergeal, F. Schackert, M. Metcalfe, R. Vijay, V.E. Manucharyan, L. Frunzio, D.E. Prober, R.J. Schoelkopf, S.M. Girvin, and M.H. Devoret, Phase preserving amplification near the quantum limit with a josephson ring modulator, Nature **465**, 64 (2010).

[22] Y.-F. Chen, D. Hover, S. Sendelbach, L. Maurer, S.T. Maerkal, E.J. Pritchett, F.K. Wilhelm, and R. McDermott, Microwave photon counter based on josephson junctions, Physical Review Letters **107**, 217401 (2012).

[23] L.C.G. Govia, E.J. Pritchett, S.T. Merkel, D. Pineau, and F.K. Wilhelm, Theory of josephson photomultipliers: Optimal working conditions and back action, Phys. Rev. A **86**, 032311 (2012).

[24] Jeffrey E Marchese, Matteo Cirillo, and Niels Grønbech-Jensen, Classical analysis of phase-locking transients and rabi-type oscillations in microwave-driven josephson junctions, Physical Review B **73**, 174507 (2006).

[25] J Claudon, F Balestro, FWJ Hekking, and O Buisson, Coherent oscillations in a superconducting multilevel quantum system, Physical Review Letters **93**, 187003 (2004).

[26] J Lisenfeld, A Lukashenko, M Ansmann, JM Martinis, and AV Ustinov, Temperature dependence of coherent

oscillations in josephson phase qubits, Physical Review Letters **99**, 170504 (2007).
[27] Niels Grønbech-Jensen and Matteo Cirillo, Rabi-type oscillations in a classical josephson junction, Physical Review Letters **95**, 067001 (2005).
[28] J. Koch, T.M. Yu, J. Gambetta, A. A. Houck, D. I. Schuster, J. Majer, A. Blais, M. H. Devoret, S. M. Girvin, and R. J. Schoelkopf, Charge-insensitive qubit design derived from the cooper pair box, Phys. Rev. A **76**, 042319 (2007).
[29] M. Tinkham, *Introduction to Superconductivity* (McGraw-Hill, New York, 1996).
[30] V. Lefevre-Sequin, E. Turlot, C. Urbina, D. Esteve, and M. H. Devoret, Thermal activation of a hysteretic dc superconducting quantum interference device from its different zero-voltage states, Phys. Rev. B **46**, 5507 (1992).
[31] Y.J. Yoon and B. Kim, A new formula for effective dielectric constant in multi-dielectric layer microstrip structure, in *IEEE Conference on Electrical Performance of Electronic Packaging* (2000) pp. 163–167.
[32] K. C. Gupta, R Garg, I Bahl, and P. Bhatia, *Microstrip Lines and Slotlines* (Artech House, MA, 1996).
[33] G. J. Dolan, Offset masks for lift-off photoprocessing, Appl. Phys. Lett. **31**, 337–339 (1977).
[34] Frank Deppe, Shiro Saito, Hirotaka Tanaka, and Hideaki Takayanagi, Determination of the capacitance of nm scale josephson junctions, Journal of Applied Physics **95**, 2607–2613 (2004).
[35] M. P. DeFeo, P. Bhupathi, K. Yu, T. W. Heitmann, C. Song, R. McDermott, and B. L. T. Plourde, Microstrip superconducting quantum interference device amplifiers with submicron josephson junctions: Enhanced gain at gigahertz frequencies, Appl. Phys. Lett. **97**, 092507 (2010).
[36] See `http://web.physics.ucsb.edu/~martinisgroup/electronics.shtml`
[37] In the linear regime of the Josephson junctions, this expression can be derived by standard circuit analysis treating individual junction inductances as $L_{J0}/\cos(\varphi)$, with φ representing the phase across each junction, or alternatively by expanding the potential energy in Eq. (1) around the minima of $\varphi_{\pm}$. The term $L_g/4$ comes from the fact that in the case of non-zero geometric inductance L_g, the voltage across the SQUID is not $\phi_0\dot{\varphi}_+$, but instead $\phi_0\dot{\varphi}_2$ (as can be seen from Fig. 5). Yet another, equivalent way of calculating L_t, would be to expand the effective potential energy discussed in the Appendix A around the minimum of φ_2.
[38] A. D. O'Connell, M Ansmann, R. C. Bialczak, M. Hofheinz, N. Katz, E. Lucero, C. McKenney, M. Neeley, H. Wang, E. M. Weig, A. N. Cleland, and J. M. Martinis, Microwave dielectric loss at single photon energies and millikelvin temperatures, Appl. Phys. Lett. **92**, 112903 (2008).
[39] Harry Nyquist, Thermal agitation of electric charge in conductors, Physical review **32**, 110–113 (1928).
[40] Herbert B Callen and Theodore A Welton, Irreversibility and generalized noise, Physical Review **83**, 34 (1951).
[41] Eshel Ben-Jacob, Emil Mottola, and Gerd Schön, Quantum shot noise in tunnel junctions, Physical Review Letters **51**, 2064 (1983).
[42] Hendrik Anthony Kramers, Brownian motion in a field of force and the diffusion model of chemical reactions, Physica **7**, 284–304 (1940).
[43] E Ben-Jacob, DJ Bergman, Y Imry, BJ Matkowsky, and Z Schuss, Thermal activation from the fluxoid and the voltage states of dc squids, Journal of applied physics **54**, 6533–6542 (1983).
[44] Siyuan Han, J Lapointe, and JE Lukens, Effect of a two-dimensional potential on the rate of thermally induced escape over the potential barrier, Physical Review B **46**, 6338 (1992).
[45] P. Hänggi, P. Talkner, and M. Borkovec, Reaction-rate theory: fifty years after kramers, Rev. Mod. Phys. **62**, 252 (1990).
[46] N. Grønbech-Jensen, MG Castellano, F. Chiarello, M. Cirillo, C. Cosmelli, LV Filippenko, R. Russo, and G. Torrioli, Microwave-induced thermal escape in josephson junctions, Physical Review Letters **93**, 107002 (2004).
[47] John Clarke, Squids: Then and now, International Journal of Modern Physics B **24**, 3999–4038 (2010).
[48] Robert McDermott, SeungKyun Lee, Bennie Ten Haken, Andreas H Trabesinger, Alexander Pines, and John Clarke, Microtesla mri with a superconducting quantum interference device, Proceedings of the National Academy of Sciences of the United States of America **101**, 7857–7861 (2004).
[49] TM Lanting, Hsiao-Mei Cho, John Clarke, WL Holzapfel, Adrian T Lee, M Lueker, PL Richards, Matt A Dobbs, Helmuth Spieler, and A Smith, Frequency-domain multiplexed readout of transition-edge sensor arrays with a superconducting quantum interference device, Applied Physics Letters **86**, 112511 (2005).
[50] D Drung, C Assmann, J Beyer, A Kirste, M Peters, F Ruede, and Th Schurig, Highly sensitive and easy-to-use squid sensors, Applied Superconductivity, IEEE Transactions on **17**, 699–704 (2007).
[51] CH van der Wal, FK Wilhelm, CJPM Harmans, and JE Mooij, Engineering decoherence in josephson persistent-current qubits, The European Physical Journal B-Condensed Matter and Complex Systems **31**, 111–124 (2003).
[52] A Lupaşcu, EFC Driessen, L Roschier, CJPM Harmans, and JE Mooij, High-contrast dispersive readout of a superconducting flux qubit using a nonlinear resonator, Physical Review Letters **96**, 127003 (2006).
[53] I. Serban, B. L. T. Plourde, and F. K Wilhelm, Quantum nondemolition-like fast measurement scheme for a superconducting qubit, Phys. Rev. B **78**, 054507 (2008).
[54] M. P. DeFeo and B. L. T. Plourde, Superconducting microstrip amplifiers with sub-kelvin noise temperature near 4ghz, Applied Physics Letters **101**, 052603 (2012).
[55] G. J. Ribeill, D. Hover, Y.-F. Chen, S. Zhu, and R. McDermott, Superconducting low-inductance undulatory galvanometer microwave amplifier: Theory, Journal of Applied Physics **110**, 103901 (2011).
[56] T. L. Robertson, B. L. T. Plourde, T. Hime, S. Linzen, P. A. Reichardt, F. K. Wilhelm, and John Clarke, Superconducting quantum interference device with frequency-dependent damping: Readout of flux qubits, Physical Review B **72**, 024513 (2005).
[57] BLT Plourde, TL Robertson, PA Reichardt, T Hime, S Linzen, C-E Wu, and John Clarke, Flux qubits and readout device with two independent flux lines, Physical Review B **72**, 060506 (2005).
[58] M.H. Devoret, Quantum fluctuations in electrical circuits, in *Quantum Fluctuations*, Les Houches Session No.

LXIII (Elsevier, Amsterdam, 1995) p. 351.